PCCP

ROYAL SOCIETY OF CHEMISTRY

PAPER

View Article Online
View Journal

Cite this: DOI: 10.1039/d5cp02385h

Crystal structure and lithium-ion diffusion mechanism in the inverse spinel solid solution series, $Li_{2+x}Ni_{2-2x}Cr_xV_2O_8$ ($0 \leq x \leq 1$)

Daniel Z. C. Martin, [a] Rebecca Boston, [a] Babatunde A. Adedayo, [a] Ronald I. Smith, [b] Peter J. Baker, [b] Maria Diaz-Lopez, [c] Veronica Celorrio [d] and Nik Reeves-McLaren *[a]

Received 23rd June 2025,
Accepted 22nd September 2025

DOI: 10.1039/d5cp02385h

rsc.li/pccp

A new solid solution series based on substitution of Cr into $LiNiVO_4$, with the stoichiometric formula $Li_{2+x}Ni_{2-2x}Cr_xV_2O_8$ ($0 \leq x \leq 1$), is reported here for the first time. The materials crystallise in the $Fd\bar{3}m$ space group as inverse spinels, with (at ambient temperatures) vanadium on the tetrahedral site and Li, Cr and/or Ni filling the octahedral interstices. High temperature neutron diffraction data are used to identify a continuous three-dimensional Li^+-ion conduction pathway along 16c–8a–16c sites, with bulk activation energies ranging from 0.17 eV for powdered specimens to 0.53 eV for samples sintered at 550–650 °C. Lithium diffusion coefficients at 300 K were calculated from muon spectroscopy data to be in the region of 2×10^{-12} cm^2 s^{-1}. Preliminary electrochemical data show significant capacity loss after first discharge when employed as positive electrodes, as is common for similar inverse spinels, but show significant promise for negative electrode applications with *ca.* 110 mAh g^{-1} in reversible specific capacity remaining after 50 cycles at an average operating potential of *ca.* 0.6 V.

1. Introduction

The ongoing pursuit for improved performance in lithium-ion batteries hinges on the discovery and optimisation of new electrode materials. In recent years, there has been much focus on the development of layered transition metal oxides, such as the Ni-rich so-called NMC compounds that offer improvements in energy density, and olivine-structured materials such as $LiFePO_4$, which deliver impressive cycling performance.[1]

Materials with the spinel crystal structure are also of significant interest, particularly for high voltage and solid-state battery applications. With the general formula AB_2O_4, spinels have a structure consisting of cubic close packed O^{2-} anions, with cations then filling one-eighth of the available tetrahedral sites, and half of the octahedral interstices as well. Depending on the distribution of the A and B cations present, the spinel structure may broadly be classified as 'normal' ($[A]_{tet}[B_2]_{oct}O_4$), 'inverse' ($[B]_{tet}[A,B]_{oct}O_4$) or 'random' ($[B_{0.67}A_{0.33}]_{tet}[A_{0.67}B_{1.33}]_{oct}O_4$). Cationic distribution has important implications on the migration pathways utilised by mobile species such as lithium, which must be continuous if (de)intercalation and/or long range migration is to allow for electrode or solid electrolytic applications.

Normal spinels, such as $LiMn_2O_4$ and $LiCoMnO_4$, have been well studied and their Li^+-ion conduction mechanisms are generally well understood, following a two-step conduction mechanism involving Li^+-ions in 8a tetrahedral sites hopping into empty 16c octahedral sites and then onto adjacent 8a sites, forming a three-dimensional pathway for ionic migration.[2] Spinel-based titanates such as $Li_4Ti_5O_{12}$ are also of interest as negative electrode materials. These spinel-based materials are particularly attractive for solid-state battery applications thanks to their excellent dimensional stability during Li (de)intercalation.[3,4]

In contrast to these well-studied normal spinels, inverse spinels have received much less attention, with migration pathways less well established and with relatively limited electrochemical properties reported. Since pentavalent vanadium has a strong preference for tetrahedral coordination, vanadate spinels tend to crystallise in the inverse cation arrangement, and $LiMVO_4$ (M = Mg, Mn, Co, Ni) systems have been studied for both positive and negative electrode applications, the latter due to the enticing possibilities for multivalent redox processes offered by presence of a $V^{5+/3+}$ couple. These systems have attracted interest as cathode materials because

[a] School of Chemical, Materials and Biological Engineering, University of Sheffield, Mappin Street Sheffield, S1 3JD, UK. E-mail: nik.reeves-mclaren@sheffield.ac.uk
[b] ISIS Facility, Science and Technology Facilities Council, Rutherford Appleton Laboratory, Harwell Science and Innovation Campus, Didcot, Oxfordshire, OX11 0QX, UK
[c] Université Grenoble Alpes, CNRS, Institut Néel, 38042 Grenoble, France
[d] Diamond Light Source, Harwell Science and Innovation Campus, Didcot, Oxfordshire OX11 0QX, UK

they operate at relatively high voltages (3.8–4.8 V *vs.* Li/Li^+) with theoretical capacities of *ca.* 148 mAh g^{-1}, depending on the transition metal choice.[5,6] However, so far only limited discharge capacities (between 40 to 90 mAh g^{-1}) and significant issues with capacity fading have been observed.[7] As negative electrodes, $LiNiVO_4$ and $LiZnVO_4$ have initial discharge capacities of between 850 to 1110 mAh g^{-1} and 1008 mAh g^{-1}, respectively.[7,8] Despite the high initial capacities observed, these materials typically suffer from huge capacity fade (>50%) during subsequent cycles. On the other hand, $LiMgVO_4$ displays a lower initial discharge capacity of 581 mAh g^{-1}, but with a capacity retention of 91% after 30 cycles. These materials also exhibit low initial coulombic efficiencies, with $LiMgVO_4$ displaying a charge capacity of *ca.* 202 mAh g^{-1}, corresponding to a coulombic efficiency of only 35%.[8] The observed differences in cycling behaviour of these materials have been attributed to different reaction mechanisms (*e.g.* intercalation or conversion-like mechanisms). Much work is required if inverse spinels are to deliver on their promise, and will rely on (i) improved understanding of how lithium ions migrate through their crystal structure, and (ii) stabilisation of the crystal structures to better survive initial deintercalation of the lithium.

Here, we report for the first time a new inverse spinel solid solution series with compositions $Li_{2+x}Ni_{2-2x}Cr_xV_2O_8$ ($0 \leq x \leq 1$), lying between two end-member phases: $LiNiVO_4$ and $Li_3CrV_2O_8$. The composition $Li_3CrV_2O_8$ was first reported in the 1960's separately by Blasse and by Joubert and Durif.[9,10] The structure was described as an inverse spinel with Li and Cr occupying octahedral sites and V occupying tetrahedral sites. However, their conclusions differed on whether 3 : 1 ordering was observed between Li and Cr on the octahedral sites. No report has previously been made of possible lithium-ion mobility or of electrochemistry in this system, a surprising omission given a theoretical capacity of 266 mAh g^{-1} based on full extraction of all three lithium cations and utilisation of the $Cr^{3+/6+}$ redox couple. As occurs for other Cr-based spinels, if this capacity was delivered at a high average operating voltage close to 5 V, this could in theory deliver very high energy densities exceeding 1300 Wh kg^{-1}, far in excess of that possible from the Ni-rich layered transition metal oxides attracting significant commercial interest – if reversible (de)lithiation were to be possible in such a lithium-rich inverse spinel system.

2. Experimental methods

2.1. Synthesis and characterisation

Samples with compositions $Li_{2+x}Ni_{2-2x}Cr_xV_2O_8$ ($0 \leq x \leq 1$) were synthesised *via* a citric acid sol–gel route. Stoichiometric amounts of $LiNO_3$ (Alfa Aesar, 99%, dried at 180 °C), $Cr(NO_3)_3 \cdot 9H_2O$ (Alfa Aesar, 99.99%), and nickel acetate tetrahydrate ($Ni(OCOCH_3)_2 \cdot 4H_2O$, Sigma-Aldrich, 99%) were dissolved in deionised water at 80 °C with constant magnetic stirring. V_2O_5 (Sigma Aldrich, 99.6%, dried at 180 °C) was then added to form a brown suspension, followed by the dropwise addition of an aqueous solution of citric acid, to give a 1 : 3 ratio by weight of metal cations to citric acid. This caused dissolution of the vanadium reagent, resulting in a clear dark blue solution, which was stirred at 120 °C until all water evaporated to leave a dried precursor. This was ground using an agate mortar and pestle, placed into an alumina crucible and calcined in air at 500 °C for 24 hours with intermittent regrinding. All heating and cooling steps were carried out at 5 °C min^{-1}.

The products were characterised by X-ray diffraction using a PANalytical X'Pert[3] Powder diffractometer using Cu Kα radiation (λ = 1.5418 Å) and MediPix detector. The ICDD's PDF-4+ database and SIeve+ software were used for phase analysis. For lattice parameter determination, data were collected in transmission geometry using a STOE STADI P diffractometer, fitted with a linear position sensitive detector and primary beam monochromator to give a highly pure Mo $K\alpha_1$ beam (λ = 0.7107 Å). A NIST 640d silicon standard reference material was added as an internal calibrant to allow correction for peak position aberrations.

Finally, for crystal structure refinements time-of-flight powder neutron diffraction data were collected both at room temperature and over the temperature range 250–600 °C on the Polaris instrument at the ISIS Neutron and Muon Facility, Rutherford Appleton Laboratory, UK.[11] For data collection at room temperature, samples with x = 0.0, 0.25, 0.5 and 0.75 were loaded into 6 mm or 8 mm diameter vanadium cans, depending on sample quantity, mounted in the diffractometer on an automatic sample changer and exposed to the neutron beam for between 120 and 175 μAh integrated proton beam current to the ISIS target (*ca.* 45 to 60 minutes each). For variable temperature work, samples with x = 0.5 and 1.0 were loaded into 8 mm internal diameter silica glass tubes and mounted inside a furnace designed for neutron diffraction experiments. The glass tubes were attached to a gas handling system that enabled dry compressed air to be passed over the powders to prevent the formation of reducing atmospheres during data collection. Data normalisation used the Mantid software, incorporating corrections to account for sample absorption effects and background scattering from sample containment.[12] Structure refinement by the Rietveld method was carried out using data collected in Polaris detector banks 3, 4, 5 (average 2θ scattering angles 52°, 92° and 146° respectively) with the EXPGUI interface for GSAS.[13,14] The estimated standard deviations (ESDs) quoted are as given by GSAS.

2.2. Impedance spectroscopy

Pellets were prepared using a cold uniaxial press, covered in a bed of sacrificial powder to minimise lithia loss, and sintered for 12 hours at 650 °C for ($0 \leq x \leq 0.75$) and 550 °C for x = 1. The densified bodies were polished and sputter-coated with gold to form electrodes on opposing faces. The coated pellets were heated under dry air to 250 °C, and the impedance of each sample measured on subsequent cooling using a Solartron 1260 impedance analyser in the frequency range of 10^6 Hz to 0.01 Hz with an applied AC bias of 100 mV. All measurements were corrected for sample geometry and analysed using the ZView software.[15]

2.3. Muon spin relaxation (μSR) spectroscopy

Muon spectroscopy data were collected using the EMU instrument at the ISIS Neutron and Muon Facility, Rutherford Appleton Laboratory, UK. Approximately 2 g of powdered specimens of x = 0, 0.5 or 1 were packed into separate Ti sample holders, forming disk-shaped samples of *ca.* 24 mm diameter and 1.5 mm thickness and retained by Ti foil windows of *ca.* 30 μm thickness. The sample environment temperature was controlled using a closed cycle refrigerator, with data collected from 100–600 K in three applied longitudinal magnetic fields of 0, 5 and 10 G. Positively-charged spin-polarised muons with energy 3.2 MeV were implanted into samples, and their subsequent decay into positrons was detected using 96 scintillator segments arranged in two circular arrays. Initial asymmetry calibrations were conducted using a 20 G transverse magnetic field at 300 K. Data analysis was conducted using the Mantid program.[12]

2.4. Electrochemical testing

Galvanostatic cycling with potential limitation was performed in Swagelok type cells (Fig. S19 in SI) using a Biologic VSP potentiostat. For both positive and negative electrode testing, 10 mm diameter pellets of approximately 20 mg of electrode material were pressed outside the glovebox and dried for *ca.* 12 h in a vacuum oven at 80 °C. The electrode mixture consisted of 75 wt% active material, 15 wt% carbon black (MTI), and 10 wt% polyvinylidene fluoride (PVDF, MTI). Half cells were then fabricated in an Ar-filled glovebox by stacking the pellets of electrode material, a Whatman glass microfibre separator, and a 10 mm diameter lithium metal disk (Sigma-Aldrich, 99%) pressed on a stainless steel plate as the counter electrode. The electrolyte solution consisted of 1 M $LiPF_6$ dissolved in ethylene carbonate (EC) and dimethyl carbonate (DMC) 1 : 1 v/v (Sigma-Aldrich, battery grade). A C-rate of C/10 was used for all experiments (where C/10 corresponds to a current that would theoretically fully charge or discharge the battery in 10 hours based on the theoretical capacity of the material) with a voltage range of 3 to 4.9 V for cathode experiments and 2.5 to 0.02 V for negative electrode experiments.

2.5. *Operando* X-ray absorption near edge spectroscopy (XANES)

XANES data were collected during electrochemical cycling on the B18 beamline at the Diamond Light Source synchrotron facility (Harwell Science & Innovation Campus, Oxfordshire, UK). All measurements were carried out in fluorescence mode, using a Si single crystal (111) monochromator. Spectra were collected on the V, Cr, and Ni K-edges of $Li_{2.75}Ni_{0.5}Cr_{0.75}V_2O_8$ and $Li_{2.5}NiCr_{0.5}V_2O_8$ as cathode materials using a multichannel potentiostat (3 to 4.9 V). Powder electrodes were prepared *via* mixing with carbon black (1 : 1 wt%) and cycled at a C-rate of C/20 for $Li_{2.75}Ni_{0.5}Cr_{0.75}V_2O_8$ and C/15 for $Li_{2.5}NiCr_{0.5}V_2O_8$. Different C-rates had to be used due to beamline time constraints. Electrochemical cells were again prepared in an Ar-filled glovebox using a specially designed cell for synchrotron radiation experiments, fitted with a Be window to allow X-ray transmission.

Additional XANES spectra were collected from standard reference materials of known valence (VO_2, V_2O_5, NiO, $LiNiO_2$, $Ni(OCOCH_3)_2{\cdot}4H_2O$, Cr_2O_3, CrO_2 and K_2CrO_4), as well as pristine uncycled powder samples of $Li_{2+x}Ni_{2-2x}Cr_xV_2O_8$ (x = 0, 0.25, 0.5, 0.75 and 1) for comparison. Samples were mixed with cellulose and pressed into 10 mm diameter pellets.

XANES spectra were normalised and calibrated against the metallic foil (V, Cr or Ni) within the Athena software package.[16] For fitting of Cr and V pre-edge regions, the program Fityk was used.[17]

3. Results and discussion

3.1. Phase formation

Room-temperature X-ray powder diffraction patterns for $Li_{2+x}Ni_{2-2x}Cr_xV_2O_8$ ($0 \leq x \leq 1$) are shown in Fig. 1. In each case, Bragg reflections could be indexed using the $Fd\bar{3}m$ space group common to cation-disordered spinels. For compositions with $x \geq 0.9$, after reaction for 24 hours some low-intensity additional reflections were also observed, which could be indexed to a Li_3VO_4 secondary phase. To optimise the reaction conditions for these Cr-rich compositions, XRD analysis was performed daily on samples heated at 500 °C. The Li_3VO_4 secondary phase was observed to gradually diminish over time, with complete disappearance achieved after 13 days (312 hours) of heating. No evidence of any Li/Cr cation ordering over octahedral sites, through *e.g.* the presence of superstructure reflections, was observed for any composition, even after long-term annealing at elevated temperatures for over 300 hours.

Refined lattice parameters are presented in Fig. 2. The data for samples reacted for 24 hours with $x \leq 0.9$ follow a linear

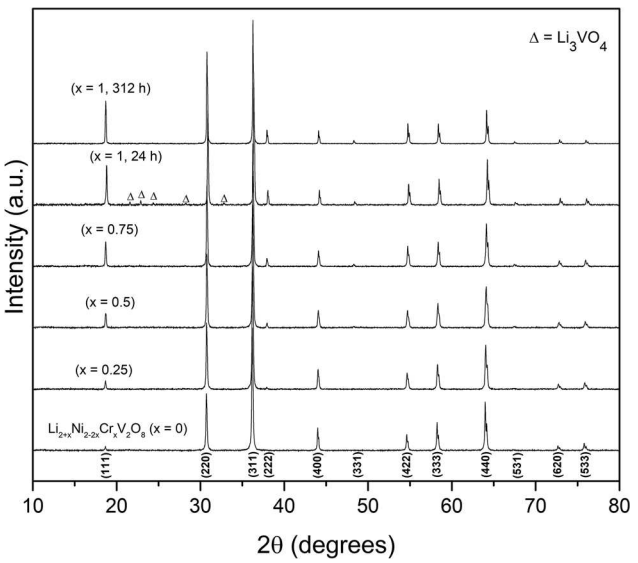

Fig. 1 XRD patterns of powdered specimens of $Li_{2+x}Ni_{2-2}Cr_xV_2O_8$ ($0 \leq x \leq 1$) following synthesis *via* a citric acid sol–gel route with final reaction at 500 °C for 12 hours unless otherwise stated.

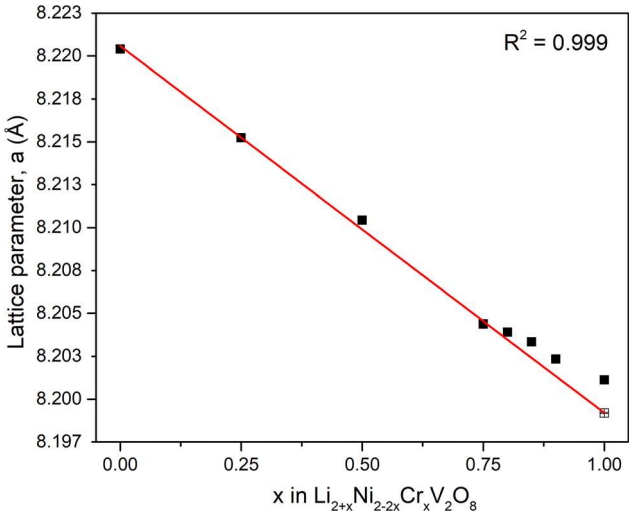

Fig. 2 Variation in lattice parameter, *a*, with composition *x* in $Li_{2+x}Ni_{2-2x}Cr_xV_2O_8$ ($0 \leq x \leq 1$). solid data points represent samples reacted at 500 °C for 24 hours; for $x = 1$, an additional unfilled data point is included for a sample annealed at 500 °C for 312 hours. estimated standard deviation is shown for, but smaller than, each data point.

trend, with a decrease in lattice parameter concomitant with the replacement of octahedrally-coordinated Ni^{2+} (ionic radius 0.69 Å) with Li^+ (0.76 Å) and the smaller Cr^{3+} (0.615 Å) cations. For the $x = 1$ composition, reaction for these relatively short times led to a deviation away from linearity, caused by the formation of the Li_3VO_4 secondary phase, meaning that the spinel phase was off-composition. However, when $x = 1$ was reacted for 312 hours, the refined lattice parameter fitted within the expected linear trend, following Vegard's Law. A complete solid solution therefore exists between $LiNiVO_4$ (which could be written as $Li_2Ni_2V_2O_8$) and $Li_3CrV_2O_8$, with the stoichiometric formula $Li_{2+x}Ni_{2-2x}Cr_xV_2O_8$ ($0 \leq x \leq 1$). Attempts at Cr-doping of $LiNiVO_4$ have been reported previously, but were not successful and so this is to our knowledge the first successful report of such.[18]

3.2. Lithium-ion conductivity

AC Impedance spectra were collected for pellets of compositions $x = 0$, 0.25, 0.5 and 0.75 sintered for 12 hours at 650 °C, and for $x = 1$ sintered for 12 hours at 550 °C. The resulting complex impedance spectra are shown in Fig. 3; sintered densities for each pellet and additional plots for capacitance and modulus spectra over a range of temperatures are included in the SI (Table S1 and Fig. S1–S5) for each composition.

In each case, the complex impedance spectra exhibit two poorly resolved arcs followed by a spike at low frequencies. The first arc, at the highest frequencies, was found to be associated with capacitance values of magnitudes *ca.* 10^{-12} F cm^{-1}, typical of a bulk (grain) response. The second arc, at intermediate frequencies and often poorly resolved from and overlapping with the first, had capacitance values of *ca.* 10^{-11} F cm^{-1}, more typically representative of a grain boundary response. At the lowest frequencies measured, and sometimes not obvious in spectra collected at lower temperatures where the response was at the limit of the measurable frequency range, a Warburg spike inclined at $>50°$ to the horizontal was observed. Its associated capacitances, with magnitudes ranging from 10^{-7}–10^{-6} F cm^{-1}, are indicative of complete or partial ionic blocking at the electrodes, indicating that these inverse spinels are Li^+-ion conductors.

Granular and total (grain and grain boundary) conductivities were extracted by fitting parallel RC elements in Zview for $x \geq 0.25$; for $x = 0$, it was not possible to reliably resolve individual semicircles and so only a total conductivity could be reasonably determined. The values obtained are broadly comparable with other materials with inverse spinel structures, such as $LiNiVO_4$ reported elsewhere (*ca.* 10^{-8} S cm^{-1}) and $LiCoVO_4$ (*ca.* 10^{-7} S cm^{-1} at 80 °C).[19] All our $Li_{2+x}Ni_{2-2x}Cr_xV_2O_8$ samples proved to be modest ionic conductors, with a total conductivity of 1.02×10^{-8} S cm^{-1} obtained at 75 °C for $x = 0$ ($LiNiVO_4$), and values increasing with Cr content to a maximum of 9.14×10^{-8} S cm^{-1} for $x = 1$. The same trend was observed for bulk conductivity, with $x = 1$ ($Li_3CrV_2O_8$) showing the highest value at 1.68×10^{-7} S cm^{-1} at 75 °C.

The samples also show typical Arrhenius-type behaviour, Fig. 4 and 5, which allowed activation energies to be determined. Activation energies were similar for all samples, falling in the range of 0.49–0.53 eV (±0.01 eV), suggesting the same mechanism is followed regardless of composition. Again, these values are reminiscent of those found in other spinel systems (*e.g.* $Li_4Ti_5O_{12}$ (0.53 eV), $LiMn_2O_4$ (0.52 eV) and $Li_2NiGe_3O_8$ (0.49 eV)), but lower than systems with lithium cations disordered over tetrahedral and octahedral positions, such as $Li_2ZnGe_3O_8$ (2.14 eV) where the ionic conduction pathway becomes blocked by transition metal cations and some of the mobile charge carrier species are effectively lost to the conduction mechanism.[20–25]

3.3. Structure refinement in the $Li_{2+x}Ni_{2-2x}Cr_xV_2O_8$ ($0 \leq x \leq 1$) solid solution series

In order to better understand the mechanism for ionic migration in these inverse spinels, crystal structure investigations were carried out using both X-ray and neutron powder diffraction data for compositions with $x = 0$, 0.25, 0.5, 0.75 and 1. Initial structural models were based on the previously reported inverse spinel structure of $LiNiVO_4$, namely with appropriate amounts of Li, Ni and Cr on octahedral 16c sites, V on tetrahedral 8b sites and oxygen on 32e sites. Site occupancies were set to sum to unity for the atom(s) occupying each crystallographic site. Initial isotropic thermal displacement parameters, U_{iso}, were fixed to a value of 0.005 Å^2, commonly found to be suitable for most inorganic oxides at ambient conditions. Lattice parameters were fixed to those determined previously from X-ray data. At each stage of refinement, parameters were allowed to vary until convergence had been achieved.

Refinements began solely with the X-ray data, refining first the scale factor and background, using a shifted Chebyshev function with 12 terms, followed by a zeropoint correction

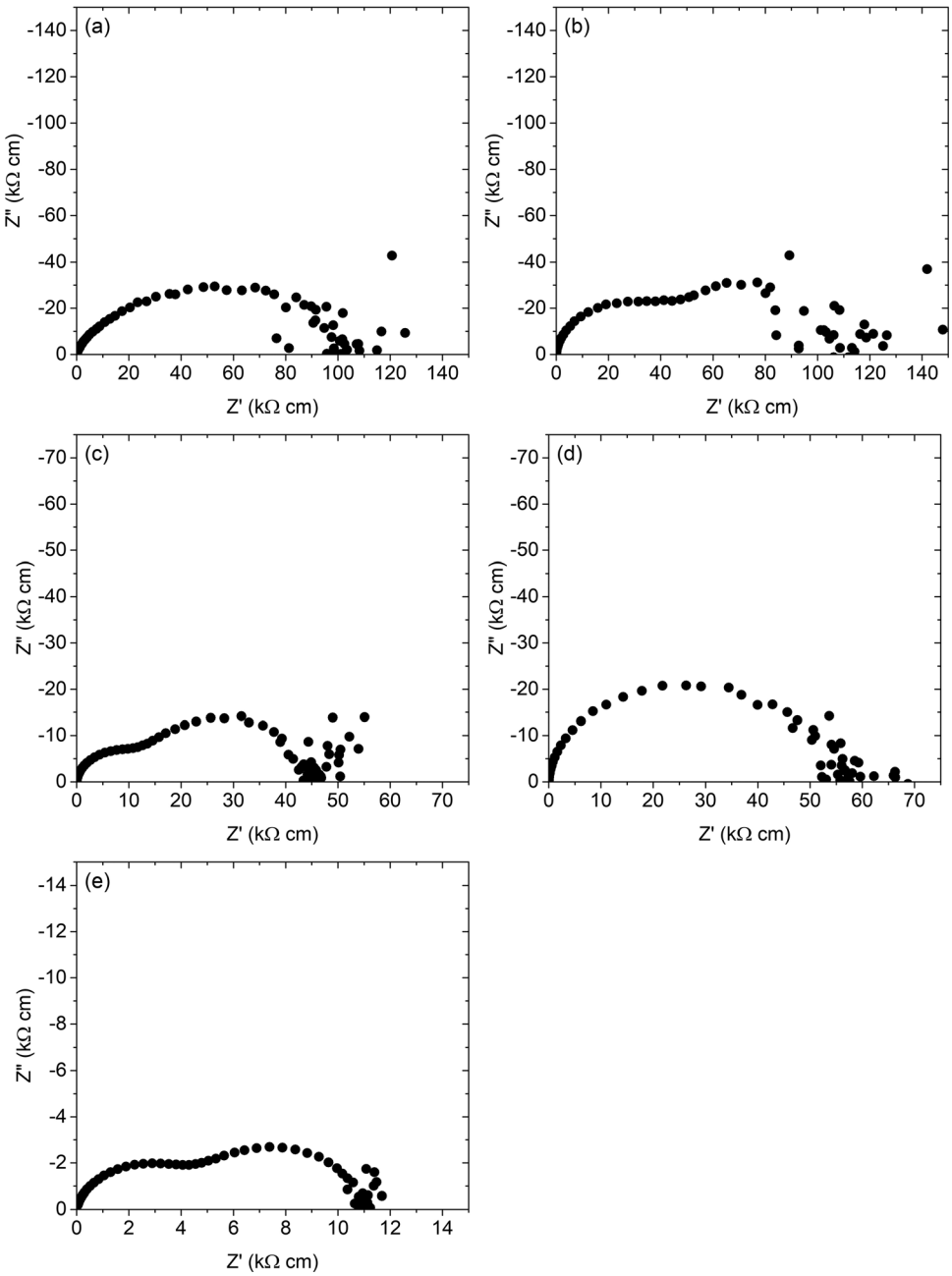

Fig. 3 Complex impedance plane plots collected at 75 °C for samples of $Li_{2+x}Ni_{2-2x}Cr_xV_2O_8$ with (a) x = 0, (b) x = 0.25, (c) x = 0.5, (d) x = 0.75 and (e) x = 1. In each instance, the frequency of measurement increases from right to left, with the highest frequency arcs corresponding to bulk responses. These are generally poorly resolved from grain boundary responses. At low frequencies in each case a Warburg spike is observed indicating that the primary conduction mechanism is ionic.

and peak width parameters. Next, the neutron datasets from the three detector banks were added, and the background and scale factors allowed to vary for these, followed by the diffractometer constant, DIFC, for the 90° and low angle bank datasets, and then peak width parameters were refined, along with DIFA to account for the wavelength dependency of neutron absorption cross-sections in a time-of-flight experiment.

For atomic parameters, refinements then used all four (X-ray and neutron) datasets. The oxygen atomic position was refined, followed by the U_{iso} parameters in order of decreasing neutron scattering length: O > [Li,Ni,Cr] > V; the U_{iso} for the mixed cation site was constrained so that all elements sharing a crystallographic site share the same thermal parameter. Finally, all parameters were gradually added and refined simultaneously until all converged and changes in the statistical measures, R_{wp} and χ^2, became negligible. This same procedure was followed for all compositions, with the only exception being for x = 0.75 where the octahedral site occupancy ($Li_{0.6875}Ni_{0.125}Cr_{0.1875}$) resulted in a relatively low number

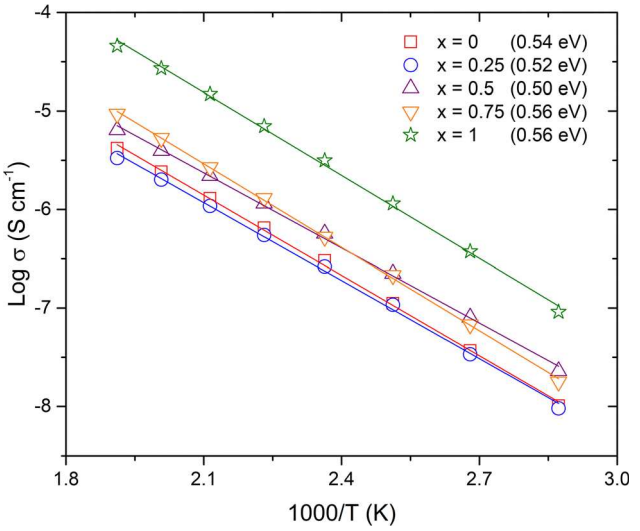

Fig. 4 Arrhenius plots of total conductivity *versus* 1000/*t* for $Li_{2+x}Ni_{2-2x}Cr_xV_2O_8$ (x = 0, 0.25, 0.5 0.75, and 1) measured under dry air. All errors were ±0.01 eV, calculated from the error in the slope.

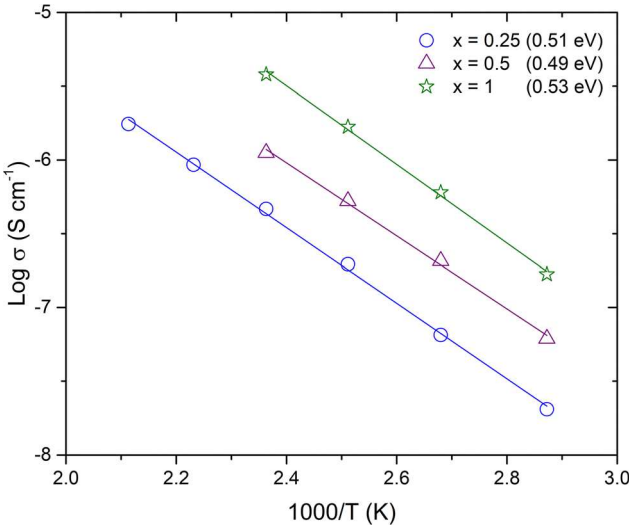

Fig. 5 Arrhenius plots of bulk conductivity *versus* 1000/*t* for $Li_{2+x}Ni_{2-2x}Cr_xV_2O_8$ (x = 0.25, 0.5, and 1) measured under dry air. All errors were ±0.01 eV, calculated from the error in the slope.

averaged neutron scattering length (+0.66 fm) for the site and made refinement of the site's thermal parameter unstable; in this case, this parameter was refined using only the X-ray data, where Ni and Cr are both strong scatterers. For x = 1, some residual reflections were observed and indexed to lithium vanadate, Li_3VO_4. Inclusion of this as a secondary phase led to a refined weight fraction of 1.5(1) %.

Final refined crystallographic parameters for each composition at room temperature are presented in Table 1, along with the resulting statistical measures. Example fitted diffraction profiles for X-ray and neutron data collected for x = 0.5 are shown in Fig. 6, with additional data for all other studied compositions available in the SI. In each case, data could be fitted using an inverse spinel crystal structure, with V solely occupying the 8b tetrahedral site, and the 16c octahedral site occupied by lithium and the transition metal(s). The fractional coordinates for the oxygen were almost unchanged regardless of composition. Interestingly, previous X-ray diffraction studies on $LiNiVO_4$ had found evidence for limited (8%) transition metal cation mixing of Ni and V over tetrahedral and octahedral sites.[26] This was not reproduced in our work; efforts to include such cation mixing led to significantly increased χ^2 (6.337) and a visibly poorer fit. Attempts to freely refine cation occupancies to introduce mixing did not lead to statistically significant deviations away from the ideal arrangement of the inverse spinel phase.

High temperature neutron powder diffraction data were collected at a range of temperatures for two compositions, up to 600 °C for x = 0.5, and up to 550 °C for x = 1. Structure refinements were conducted using the highest temperature datasets first, with the room temperature structures as the starting structural models in each case. Again, thermal parameters were set to starting values of 0.005 Å^2; it should be noted that while these values are too small for data collected at such elevated temperatures where significant atomic vibration can reasonably be expected, attribution of density in this way allows for identification of intermediate sites in the Li-ion conduction pathway. Refinements proceeded as per the previous description; background, scaling, profile and structural parameters were refined in turn, and then Fourier difference maps, Fig. S10, were generated in GSAS. Thermal parameters could not be sensibly refined for vanadium, often giving very slightly negative responses statistically indistinguishable from positive values, due to the low neutron scattering length of V, and for the purposes of identifying the lithium-ion conduction mechanism the U_{iso} for the V site was therefore kept fixed at 0.005 Å^2.

For both x = 0.5 and 1, significant negative density was located at fractional coordinates of approximately 0.125, 0.125, 0.125, equivalent to an 8a tetrahedral site unoccupied within the initial structural model, Fig. S10. No other atoms were found to be near this position, and since the neutron scattering lengths of Cr, Ni and O are all positive (3.635, 10.3 and 5.80 fm, respectively), these cannot explain this additional feature. This leaves two possible candidates for partial occupancy of a site at this new position: Li (−1.90 fm) and V (−0.39 fm); lithium is the more likely mobile species, and given the much smaller scattering length of V it is unlikely that a partially occupied vanadium site would be so easily distinguished from the residual background density. Therefore, an additional tetrahedrally-coordinated lithium site was included for further refinements, and led to improvements in both the visual fit and statistical measures.

For structure refinement of this final model with two lithium sites, the previously-described strategy was followed. Towards the end of refinements, thermal parameters were refined for the 16c site, and then fixed. Following simultaneous refinement of all other relevant parameters, the fractional

Table 1 Refined structure parameters and bond lengths from combined neutron and X-ray refinements for $Li_{2+x}Ni_{2-2x}Cr_xV_2O_8$ at 25 °C

	Atom	Site	$x = y = z$	Occ.	U_{iso}/Å^2
x = 0	V	8b	0.375	1	0.0047 (5)
a = 8.2204 (1) Å;	Li	16c	0	0.5	0.00361 (5)
R_{wp} = 2.47% χ^2 = 2.323	Ni	16c	0	0.5	0.00361 (5)
	O	32e	0.2531 (1)	1	0.00773 (4)
x = 0.25	V	8b	0.375	1	0.0052 (5)
a = 8.2152 (1) Å;	Li	16c	0	0.5625	0.00292 (6)
R_{wp} = 2.59% χ^2 = 2.594	Ni	16c	0	0.3750	0.00292 (6)
	Cr	16c	0	0.0625	0.00292 (6)
	O	32e	0.2530 (1)	1	0.00826 (4)
x = 0.5	V	8b	0.375	1	0.0057 (5)
a = 8.2104 (1) Å;	Li	16c	0	0.625	0.00099 (9)
R_{wp} = 2.76% χ^2 = 2.729	Ni	16c	0	0.250	0.00099 (9)
	Cr	16c	0	0.125	0.00099 (9)
	O	32e	0.2529 (1)	1	0.00928 (5)
x = 0.75	V	8b	0.375	1	0.0067 (6)
a = 8.2044 (1) Å;	Li	16c	0	0.6875	0.00287 (7)
R_{wp} = 3.43% χ^2 = 3.385	Ni	16c	0	0.1250	0.00287 (7)
	Cr	16c	0	0.1875	0.00287 (7)
	O	32e	0.2527 (1)	1	0.01042 (5)
x = 1	V	8b	0.375	1	0.0045 (6)
a = 8.2011 (1) Å;	Li	16c	0	0.75	0.0329 (10)
R_{wp} = 3.84% χ^2 = 2.377	Cr	16c	0	0.25	0.0329 (10)
	O	32e	0.2525 (1)	1	0.01136 (6)

Bond lengths	V_{8b}–O *4/Å	$(Li/Ni/Cr)_{16c}$–O *6/Å
x = 0	1.7362 (4)	2.0806 (3)
x = 0.25	1.7360 (5)	2.0787 (3)
x = 0.5	1.7365 (6)	2.0766 (4)
x = 0.75	1.7375 (7)	2.0739 (4)
x = 1	1.7395 (12)	2.0713 (7)

occupancy of Li was allowed to vary, giving values of 0.587(2) for x = 0.5 at 600 °C and 0.668(5) for x = 1 at 550 °C. This decrease of *ca.* 4 to 8% in site occupancy can be attributed to thermally activated hopping of lithium ions. The occupancy for the second Li site was then refined, giving values of 0.04(1) and 0.05(1) or *ca.* 4 to 5% for x = 0.5 and 1, respectively. Finally, fractional occupancies for both Li sites were then refined together with the atomic coordinates and thermal parameter for oxygen. The new structural models showed improved fits and statistical measures (lower R_{wp} and χ^2) when compared to the initial structural model. The final refined crystal structures for x = 0.5, determined at 600 °C, and x = 1, at 550 °C, are presented in Table 2, with fitted diffraction profiles for data collected in (the backscattering) bank 5 shown in Fig. 7.

The refined structures include the additional lithium site, tetrahedrally-coordinated by oxygen anions, with relatively short Li–O bond lengths of *ca.* 1.84 Å and improbably short Li_{8a}–Li_{16c} nearest neighbour distances of *ca.* 1.79 Å indicative that neighbouring sites could not be simultaneously occupied, as often seen in other Li-ion conductors.[25,27] The new 8a site shares faces with four neighbouring 16c sites, Fig. 8, resulting in a three-dimensional 16c–8a–16c conduction pathway, and explaining how reasonable levels of Li-ion conductivity can be achieved even when the 16c site is shared by Ni and/or Cr.

This approach was then extended to data collected at lower temperatures and in each case, the same additional lithium position was observed in Fourier maps and could be successfully incorporated into refinements. Key refined parameters are shown in Fig. 9 for $Li_3CrV_2O_8$, and included in the SI for $Li_{2.5}NiCr_{0.5}V_2O_8$.

For both x = 0.5 and x = 1, a linear increase in lattice parameters with temperature was observed. Given that the thermal parameters and bond lengths also increased linearly with temperature, there is no evidence in our refinements of any cation mixing or (dis)ordering and that, lithium-ion conduction aside, the standard inverse spinel model describes the average structure well at all temperatures.

A small but linear decrease in the fractional occupancy of Li on the 16c site with increasing temperature was noted for both compositions studied, consistent with the rate of ionic hopping increasing with temperature resulting in lithium cations spending less time, on average, on the standard crystallographic position occupied at room temperature. In each case, around a 5% occupancy, within errors, by lithium was seen for the newly observed 8a position.

3.4. Investigation of intra-grain diffusion by μSR

To explore lithium-ion diffusion in these inverse spinels in detail, muon spectroscopy, μSR, experiments were performed.

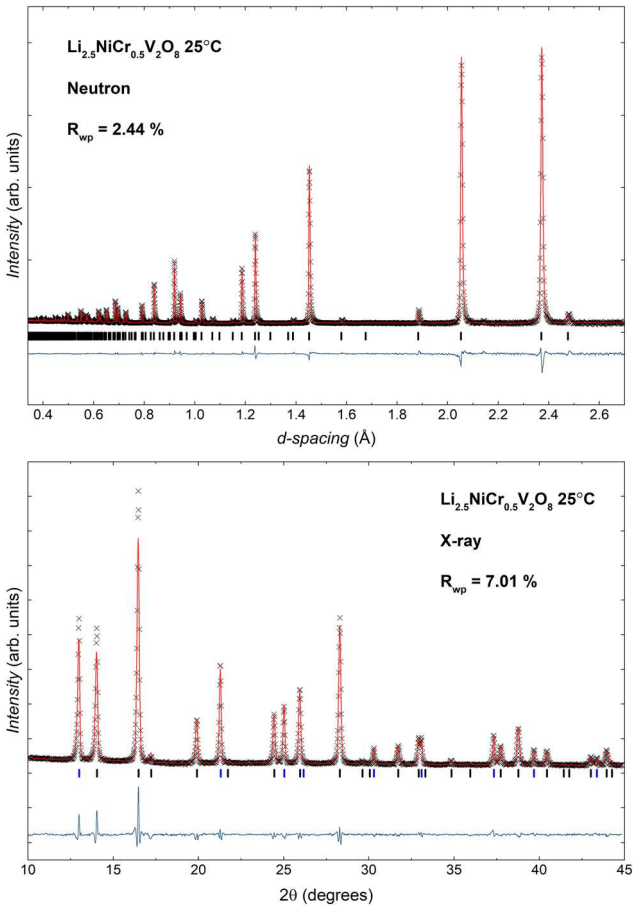

Fig. 6 Fitted powder tof neutron (bank 5) and X-ray diffraction profiles following combined structure refinement for $Li_{2.5}NiCr_{0.5}V_2O_8$ at 25 °C. Observed data points are shown as black crosses, calculated profiles as red lines, difference profile (obs-calc) as blue lines and allowed reflection positions as black (spinel phase) and blue (si standard) vertical bars.

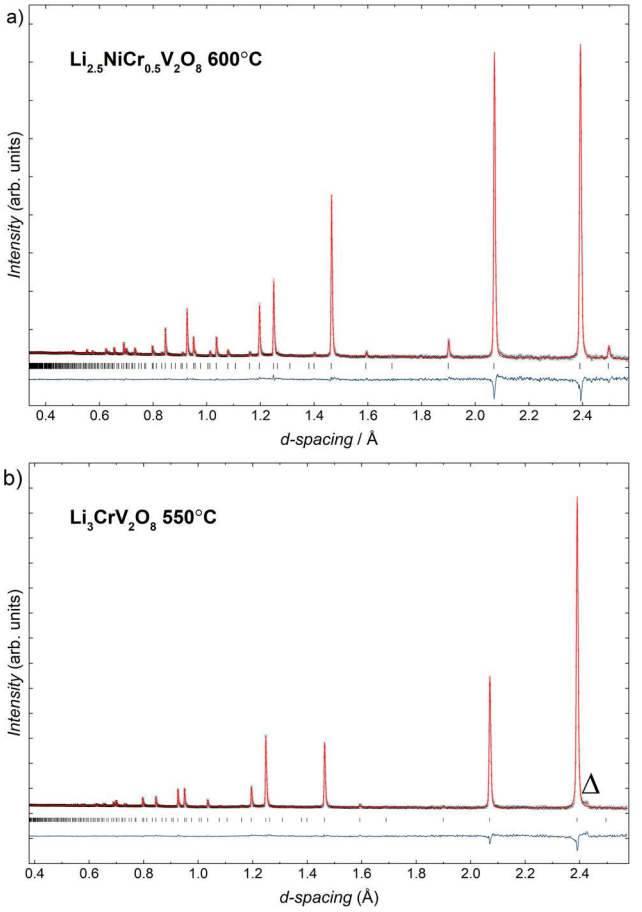

Fig. 7 Fitted powder tof neutron diffraction profiles following combined structure refinement for (a) $Li_{2.5}NiCr_{0.5}V_2O_8$ at 600 °C, and (b) $Li_3CrV_2O_8$ at 550 °C using two discrete crystallographic sites for Li. Observed data points are shown as black crosses, calculated profiles as red lines, difference profile (obs-calc) as blue lines and allowed reflection positions as black vertical bars. δ marks the presence of 1.5(1) wt% Li_3VO_4 secondary phase.

The application of muons to study the migration of positively charged cations with magnetic moments is well described elsewhere.[20,28–32] Muon decay asymmetry data were collected in longitudinal magnetic fields of 0, 5 and 10 G for x = 0, 0.5 and 1 at various temperatures, and then fitted in the WiMDA

Table 2 Refined structure parameters and calculated bond lengths for $Li_{2.5}NiCrV_2O_8$ (x = 0.5) at 600 °C and $Li_3CrV_2O_8$ (x = 1) at 550 °C, using neutron diffraction data. In both refined structural models, lithium occupies two discrete crystallographic sites within the inverse spinel structure

	Atom	Site	$x = y = z$	Occ.	U_{iso}/Å^2
x = 0.5	V	8b	0.375	1	0.005
a = 8.27819 (2) Å;	Li	16c	0	0.583 (2)	0.00284 (13)
R_{wp} = 2.50% χ^2 = 3.862	Ni	16c	0	0.250	0.00284 (13)
	Cr	16c	0	0.125	0.00284 (13)
	O	32e	0.2538 (1)	1	0.02079 (7)
	Li	8a	0.125	0.04(1)	0.005
x = 1	V	8b	0.375	1	0.005
a = 8.27280 (10) Å;	Li	16c	0	0.668 (5)	0.1061 (21)
R_{wp} = 2.64% χ^2 = 3.555	Cr	16c	0	0.125	0.1061 (21)
	O	32e	0.2533 (1)	1	0.02271 (7)
	Li	8a	0.125	0.05(1)	0.005

Bond and atom distances	V_{8b}–O *4/Å	$(Li/Ni/Cr)_{16c}$–O *6/Å	Li_{8a}–O * 4/Å	Li_{16c}–Li_{8a}/Å
x = 0.5	1.7383 (7)	2.1012 (4)	1.8463 (7)	1.7923 (1)
x = 1	1.7447 (9)	2.0953 (6)	1.8357 (9)	1.7911 (1)

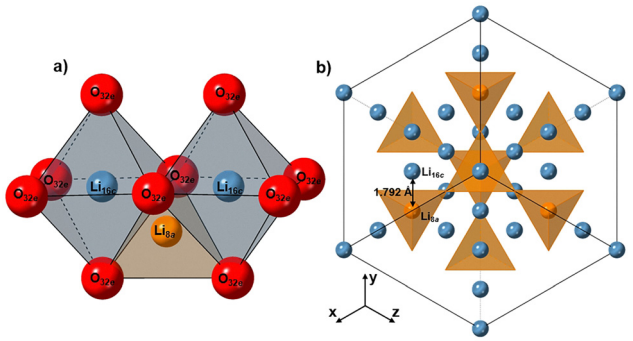

Fig. 8 (a) Portion of the $Li_{2+x}Ni_{2-2x}Cr_xV_2O_8$ (x = 0.5 and 1) inverse spinel crystal structure, showing the possible li-ion conduction pathway through the octahedra face of Li_{16c} sites (blue) into intermediate li8a sites (orange); (b) simplified crystal structure, orientated in the {111} plane, showing all possible Li positions in the unit cell. Each 16c site is surrounded by two Li_{8c} sites, and each Li_{8a} site is surrounded by four 16c sites randomly occupied by Li, Ni and/or Cr. All other atoms within the crystal structure were omitted for clarity.

software. For each temperature, the data were fitted using a single model, first using a Gaussian fit followed by a dynamic Kubo–Toyabe (DKT) function, as described by:

$$(t) = \mathrm{AG}^{\mathrm{DKT}}(\Delta, \nu, t, H_{\mathrm{LF}}) \times \mathrm{e}^{(-\lambda t)} + A_{\mathrm{BG}}$$

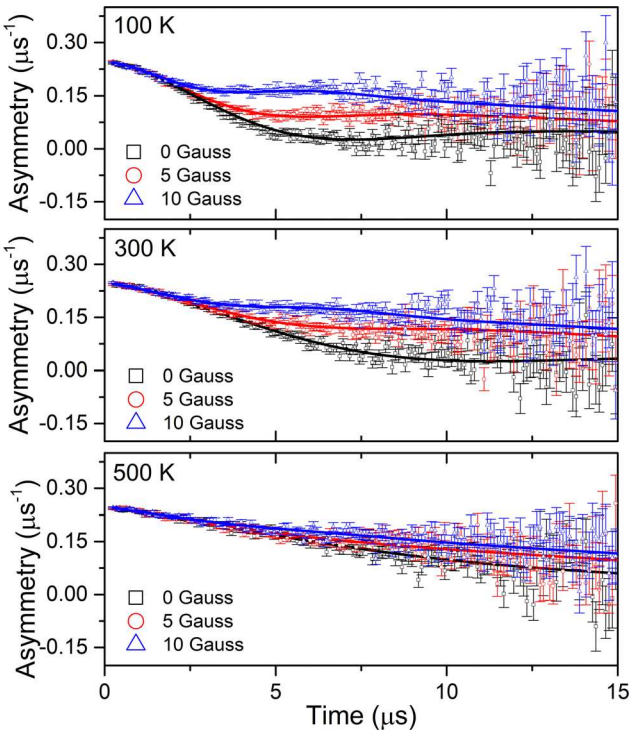

Fig. 10 Raw Muon spectroscopy data for $Li_3CrV_2O_8$, collected at 100 K, 300 K and 500 K in a zero field (squares), and applied longitudinal fields of 5 g (circles) and 10 g (triangles).

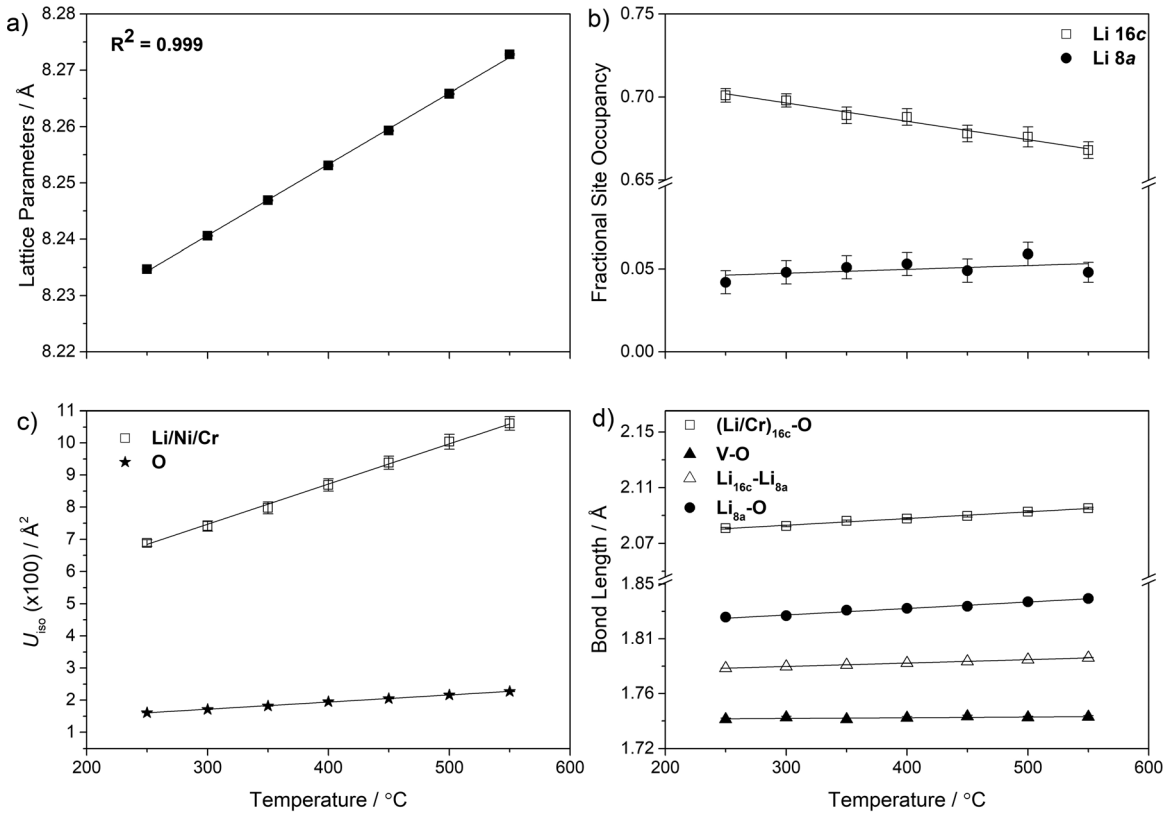

Fig. 9 Structural evolution of $Li_3CrV_2O_8$ with temperature, (a) lattice parameters, (b) fractional site occupancy of Li in 16c and 8a sites, (c) thermal displacement parameters and (d) variation of bond lengths. Some estimated standard deviations are smaller than the symbols.

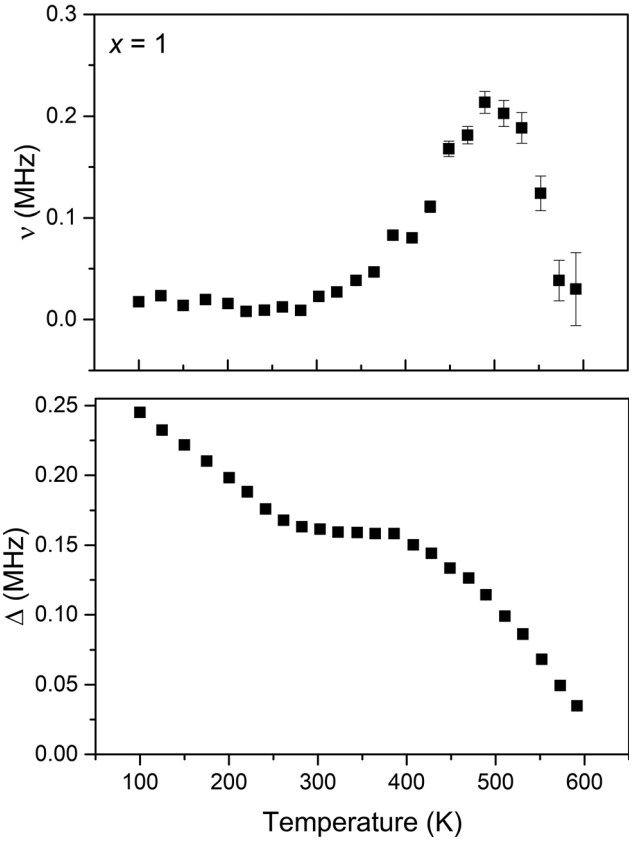

Fig. 11 Variation of ν and Δ with temperature obtained from the fitting of raw asymmetry data to equation 5.1 for $Li_3CrV_2O_8$, x = 1, measured from 100 K to 600 K.

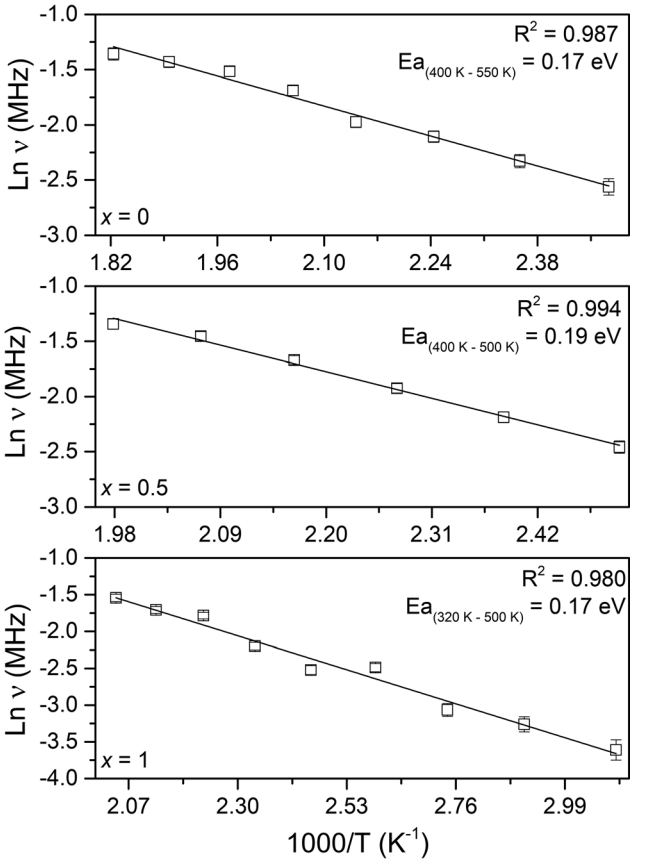

Fig. 12 Arrhenius plot of ν (mhz) *vs.* 1000/t (k – 1) of the thermally activated region for the inverse spinel series, $Li_{2+x}Ni_{2-2x}Cr_xV_2O_8$, x = 0, 0.5 and 1. The error in the activation energy was calculated to be 0.01 eV for all compositions.

The exponential term allows for modelling of the paramagnetic response associated with the unpaired electrons of Ni^{2+} and Cr^{3+}, and the final term accounts for muons stopped by the titanium sample holder. This allows separation of the DKT terms describing key parameters for ionic migration: the local field distribution, Δ, and the fluctuation rate, ν, for lithium-ions. Example fitted data for $Li_3CrV_2O_8$ are shown in Fig. 10, with the variation of the local field distribution, Δ, and the fluctuation rate, with temperature in Fig. 11.

In many lithium-ion conducting materials, *e.g.* $LiCoO_2$, $Li_2NiGe_3O_8$, the fluctuation rate shows a low temperature plateau followed by an Arrhenius-like increase; this is generally accompanied by constant values of Δ at low temperatures, which then decreases as ion hopping becomes thermally activated.[20,32,33] The data for the inverse spinels studied here differ from this standard model - instead, looking at both ν and Δ for x = 0, 0.5 and 1 we observe instead three regions: (i) a plateau in ν and a decrease in Δ at low temperatures (*ca.* 100–280 K for x = 1), which has not previously been seen in reported battery materials, (ii) a plateau in both ν and Δ at intermediate temperatures, up to *ca.* 400 K, and then (iii) above 400 K, where ν increases while Δ decreases, as typically seen for thermal activation of lithium-ion hopping. Arrhenius plots for ν, Fig. 12, over this third region allow extraction of activation energies for bulk lithium-ion conduction, with similar values of 0.17–0.19 (0.01) eV obtained for all compositions studied. Again, this indicates that the mechanism for conduction is likely very similar regardless of composition, but it should be noted that the values are significantly lower than those extracted from our electrical impedance measurements. Such discrepancies are not unusual, and in this instance likely indicate that while the barrier for ionic hopping is low, longer range migration required for ionic conductivity may be more difficult due to the mixed lithium/metal occupancy of 16c sites. At the highest temperatures the apparent value of ν decreases as the dynamics are too fast to be effectively described by the DGKT function.

Finally, the lithium-ion diffusion coefficient, D_{Li}, for $Li_{2+x}Ni_{2-2x}Cr_xV_2O_8$ (x = 0, 0.5 and 1) can be calculated using the equation:

$$D_{\mathrm{Li}} = \sum_{i=1}^{n} \frac{1}{N_i} Z_{v,i} S_i^2 \nu$$

In this, N_i is the number of available sites calculated from the three-dimensional 16c–8a–16c conduction pathway, where our refined structural models show each 16c site to be surrounded by two 8a sites. $Z_{\nu,i}$ is the vacancy fraction of destination sites, assumed to be 1 at 300 K. S_i is the hopping distance

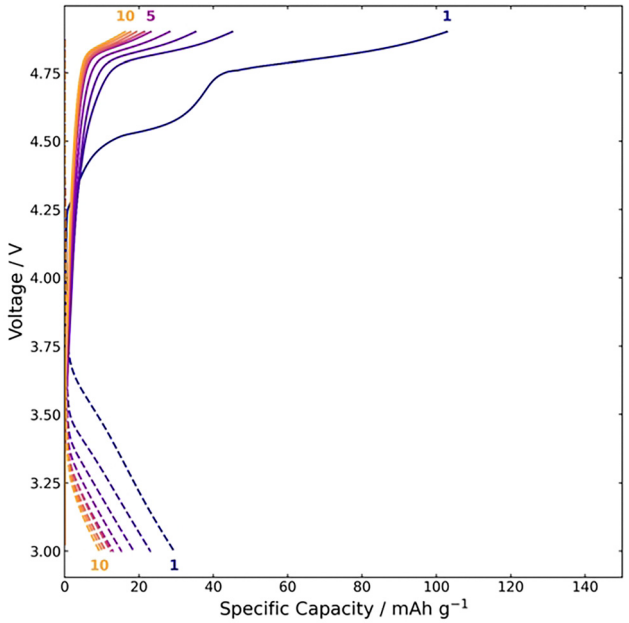

Fig. 13 Electrochemical data for $Li_{2+x}Ni_{2-2x}Cr_xV_2O_8$ (x = 0.75) for the first 10 charge and discharge cycles when cycled between 3 V and 4.9 V at C/10 rate. data for compositions x = 0, 0.25, 0.5 and 1.0 are included in the supplementary information.

between 16c and 8a sites – calculated from our neutron diffraction data to be 1.79 Å. Finally, ν is the fluctuation rate, calculated from our muon data by extrapolating the Arrhenius plots of the thermally activated region down to 300 K. By combining information from the different techniques in this way, we are able to calculate diffusion coefficients of 2.36×10^{-12} cm^2 s^{-1} for x = 0, 2.25×10^{-12} cm^2 s^{-1} (x = 0.5) and 1.96×10^{-12} cm^2 s^{-1} (x = 1). It should be noted that the diffusion coefficients calculated from μSR represent self-diffusion coefficients and do not account for thermodynamic enhancement factors or activity coefficients that may affect macroscopic ionic transport, but these results are comparable to previous work on the complex spinel, $Li_2NiGe_3O_8$ and have similar activation energies for local Li-ion diffusion to the Li-stuffed garnet, $Li_{6.5}Al_{0.25}La_{2.92}Zr_2O_{12}$ and the normal spinel, $Li_4Ti_5O_{12}$.[20,31,34] This suggests that these inverse spinels are modest lithium-ion conductors despite the mixed occupancy of 16c sites and that extraction of Li should be possible along a continuous three-dimensional migration pathway.

3.5. Electrochemical testing

3.5.1. Positive electrode performance. Electrochemical data were collected during galvanostatic cycling over 10 cycles with potential limitation between 3.0 and 4.9 V using $Li_{2+x}Ni_{2-2x}Cr_xV_2O_8$ as positive electrodes (x = 0, 0.25, 0.5, 0.75, 1), Fig. 13 and Fig. S14. For x = 0, initial charge capacities of 80 mAh g^{-1} were obtained, with very poor reversibility on discharge or further cycling. This is in good agreement with previous reports on $LiNiVO_4$, where poor reversibility is typically attributed to initial activity on the $Ni^{2+/3+}$ redox couple

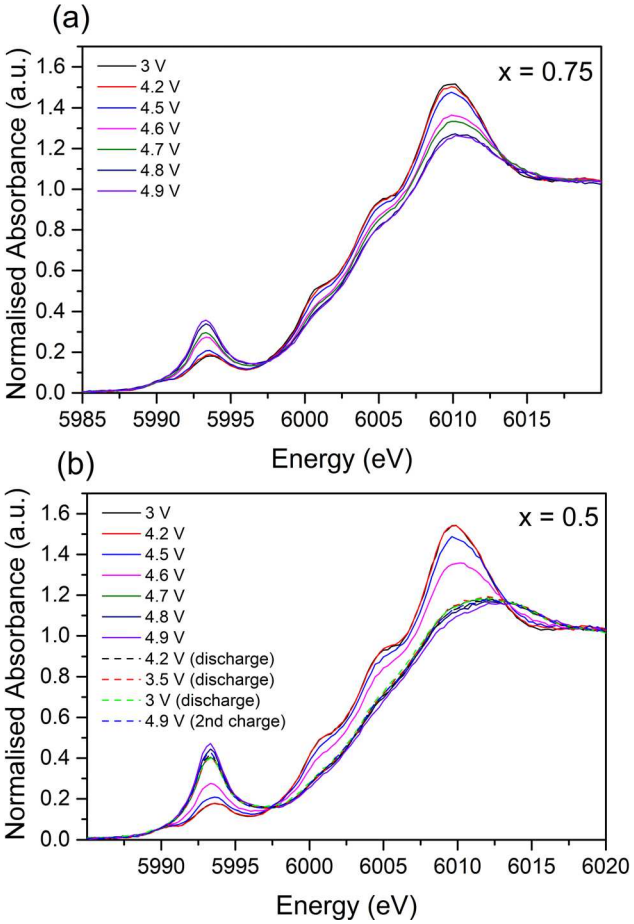

Fig. 14 Normalised Cr k-edge XANES spectra collected *in situ* during charging from 3.0 to 4.9 V for (a) x = 0.75 and (b) x = 0.5. Cells were cycled at different rates due to time constraints: C/15 for x = 0.75 and C/20 for x = 0.5.

being diminished due to (i) electrolytic degradation on cycling at potentials above 4.7 V and (ii) mixing of $Ni^{2+/3+}$ and V^{5+} cations over octahedral and tetrahedral sites on extraction of the lithium, with subsequent blocking of the cationic migration pathway.[5,7,18,35] By the 10th (dis)charge cycle, cells were effectively electrochemically inactive, delivering specific capacities below 5 mAh g^{-1}.

For x = 0.25, 0.5, and 0.75, a similar pattern was observed with 1st cycle charge capacities between 130 to *ca.* 80 mAh g^{-1}. However, two plateaus were observed during charge, at *ca.* 4.5 V and 4.8 V. The first voltage plateau shifts to lower voltages with increasing Cr content. These can likely be attributed to activity on the $Cr^{3+/6+}$ and $Ni^{2+/3+}$ couples. These processes appear largely irreversible, with discharge capacities limited to between 23 to 9 mAh g^{-1}.

To investigate these poor cycling performances, Cr, V and Ni K-edge XANES data were collected *in situ* during the first two charge cycles for compositions x = 0.75 and 0.5, Fig. S15. The Cr K-edge data, Fig. 14, showed the most significant changes on lithium extraction. Following the method described by Farges, chromium speciation in our electrode materials was

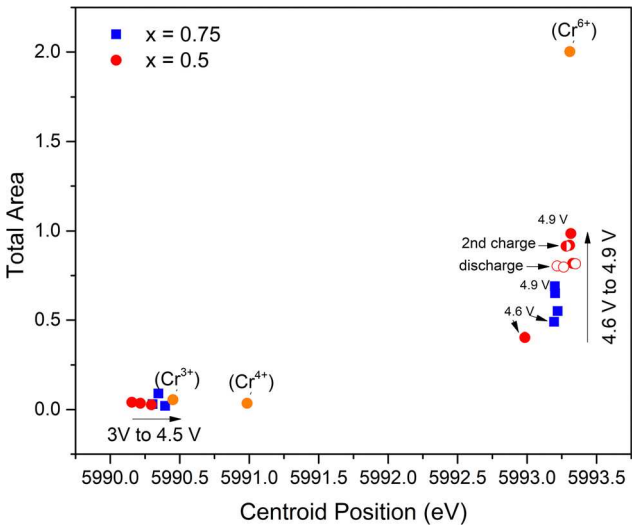

Fig. 15 Summary of pre-edge information for Cr k-edge XANES spectra collected *in situ* during cycling. Data for Cr standard reference materials are shown in orange circles, with data for x = 0.75 in blue squares and x = 0.5 data as red circles. Discharge and 2nd charge data in open and half-closed circles, respectively.

determined by comparison (Fig. S16) of centroid position and area of lower energy pre-edge features against those collected for Cr_2O_3 (Cr^{3+}), CrO_2 (Cr^{4+}) and K_2CrO_4 (Cr^{6+}) reference materials.[36]

For both compositions, on charging from 4.5 to 4.9 V there is observable shift of the Cr edge position to higher energies, with the second of two pre-edge features growing in intensity and area. Peak fitting using Fityk showed a slight shift in the centroid position on charging from 3 to 4.5 V, followed by a much more significant shift of almost 3 eV as charging continued to 4.9 V, Fig. 15. Comparison with Cr-containing standards suggests this is consistent with an increase in the average Cr valence from 3+ initially towards 6+. These changes in pre-edge features, alongside the shift to higher energies in the edge position suggests that, on charge, Cr^{3+} is oxidised to Cr^{6+} as Li-ions are extracted and Cr^{6+} ions shift from octahedral to tetrahedral sites in the inverse spinel structure.

A similar approach was taken for analysis of V K-edge XANES spectra, Fig. S17, though in this case complicated by limited availability of reliable reference compounds with V^{5+} in a range of coordination environments. For example, V_2O_5 has V^{5+} in V_2O_5 is in a square pyramidal coordination, rather than the tetrahedral coordination anticipated in an inverse spinel – this change in local structure leads to a shift in edge position of *ca.* 1 eV. Comparison was made instead against spectra in previous reports for V K-edge XANES spectra of differing oxidation states and environments.[37,38] When compared to previous analysis of differing V containing species by Chaurand *et al.*, who also observed a similar 1 eV, this suggested V in $Li_{2+x}Ni_{2-2x}Cr_xV_2O_8$ compositions is present as tetrahedrally-coordinated V^{5+}.[26,37,39]

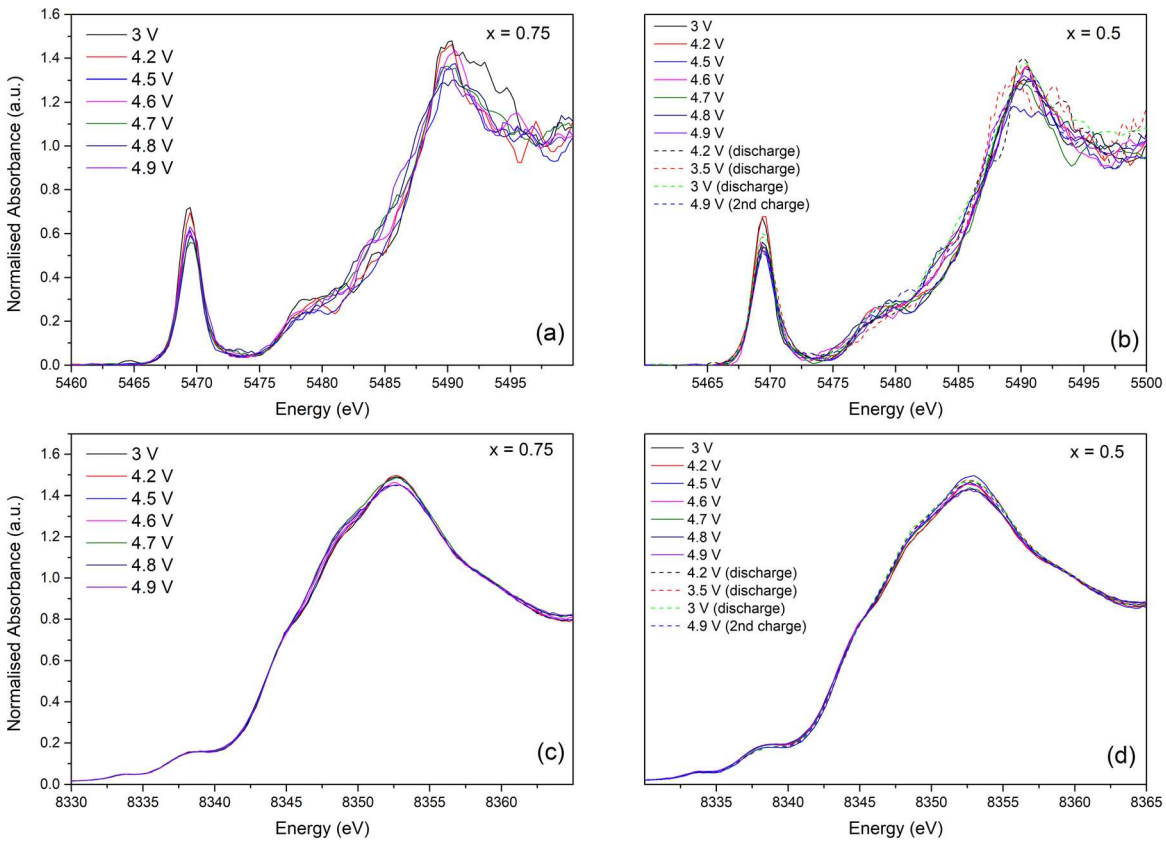

Fig. 16 Normalised (a) and (b) V k-edge and (c) and (d) Ni k-edge XANES spectra collected *in situ* during electrochemical cycling between 3 and 4.9 V for (a) and (c) x = 0.75 at C/20, and for (b) and (d) x = 0.5 at C/15.

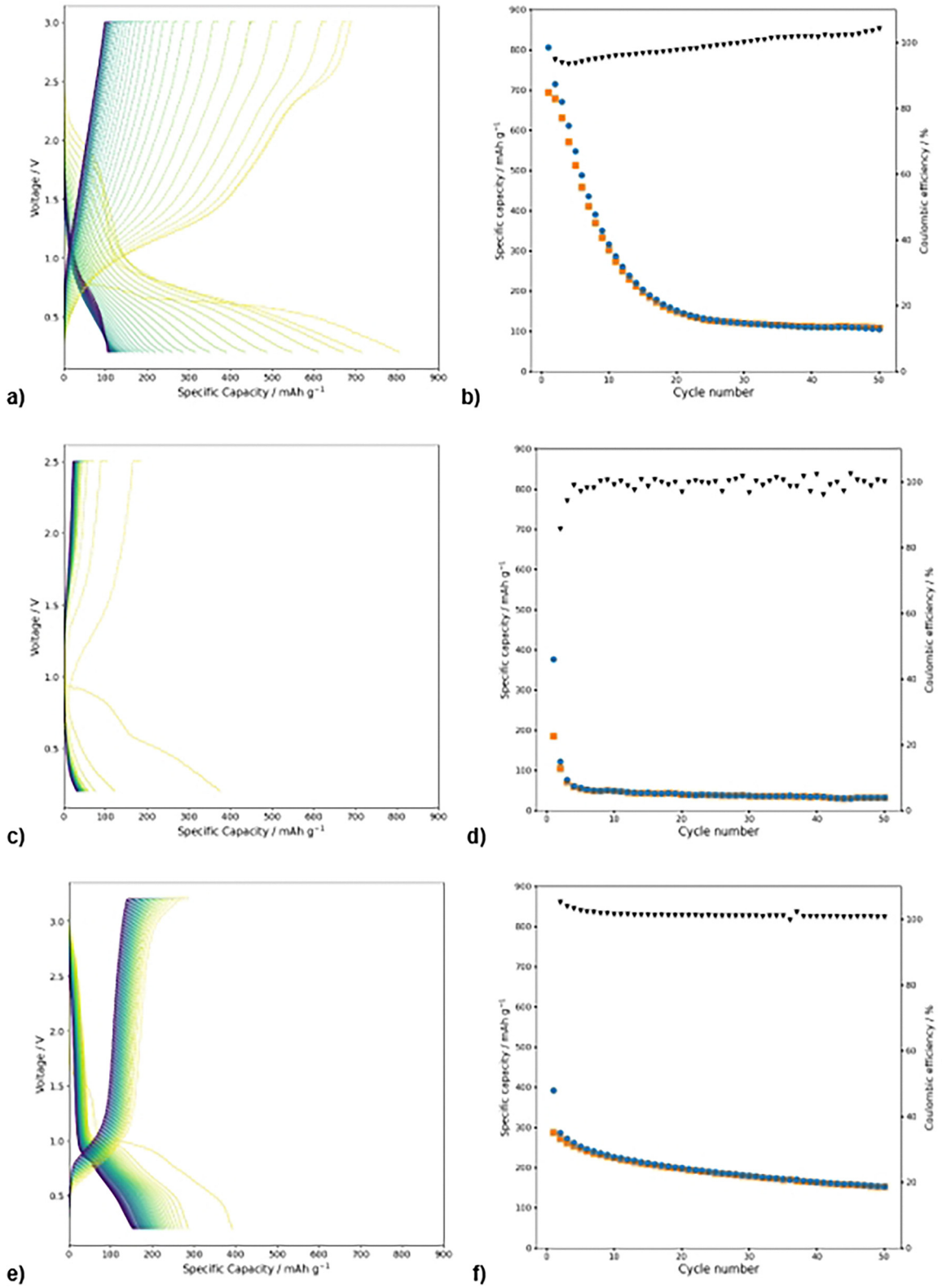

Fig. 17 Electrochemical data for (a) and (b) $LiNiVO_4$ (x = 0), (c) and (d) $Li_{2.5}NiCr_{0.5}V_2O_8$ (x = 0.5) and (e) and (f) $Li_3CrV_2O_8$ cycled as negative electrodes to 0.2 V at a rate of C/10.

On cycling, a small decrease in the pre-edge peak is observed on charge for x = 0.5 and 0.75; however, no systematic trend in the edge position is observed, Fig. 16. This likely indicates that the valence of V does not change, but that a small percentage of V^{5+}

ions may shift into octahedral sites on Li extraction, as previously suggested occurs in similar inverse spinel compounds.[26,39]

For the Ni K-edge XANES, comparisons were made, Fig. S18, with $Ni^{2+}O$, $LiNi^{3+}O_2$ (both with Ni in octahedral coordination) and $Ni^{3+}(OCOCH_3)_2{\cdot}4H_2O$ (with Ni in distorted octahedral coordination), with the closest match being to the last. There is no change in XANES spectra for x = 0.5 and 0.75 during cycling, Fig. 16, and so it is likely that Ni in $Li_{2+x}Ni_{2-2x}Cr_xV_2O_8$ remains diivalent and in a distorted octahedral environment, possibly due to Li, Cr and perhaps V sharing the same crystallographic site, throughout cycling. Ni appears to be electrochemically inactive in our Cr-rich specimens.

In summary, the electrochemical extraction of lithium is largely irreversible likely due to the migration of Cr^{6+} ions from octahedral 16c to neighbouring tetrahedral 8a sites, with some evidence of V^{5+} migrating to the 16c sites in replacement. This significantly impedes the Li^+-ion (16c–8a–16c) conduction pathway discussed in section 3.3, preventing easy reinsertion of the lithium. A similar $Cr^{3+/6+}$ redox process has been reported for the normal spinel series, $LiMn_{2-x}Cr_xO_4$, where again capacity retention on cycling was a considerable issue.[40] Work is now ongoing to add further dopants in order to attempt to prevent Cr migration.

3.5.2. Negative electrode performance. Previous studies of the $LiMVO_4$ (M = Ni, Cu, Zn and Mg) systems have shown the possibility of a two-electron $V^{5+/3+}$ redox process as a route to possible anodic behaviour, with a theoretical capacity for $LiNiVO_4$ of 297 mAh g^{-1} - significantly greater than other spinels such as $Li_4Ti_5O_{12}$.[8,39,41] Fig. 17 shows (dis)charge curves for x = 0, 0.5 and 1 cycled as negative electrodes over the voltage range 2.5 - 0.02 V.

For x = 0, the results are in good agreement with previous reports for $LiNiVO_4$.[7,39] On first discharge the voltage drops rapidly to 0.9 V, then Li insertion occurs over two main regimes from (i) a short plateau of around 100 mAh g^{-1}, followed by (ii) a longer plateau centred at around 0.65 V, associated with around 300 mAh g^{-1} capacity. These regions are separated, and followed below 0.6 V, by regions of more rapid decrease. However, on subsequent charge and (dis)charge cycles, these plateaus are not strongly observed, with a more gradual sloping change from 2 to 0.2 V indicating a likely change in insertion mechanism following the initial discharge. Observed discharge capacities drop rapidly from a total of almost 900 mAh g^{-1} in the first cycle to 406 mAh g^{-1} on the 5th cycle, all significantly higher than can be attributed to activity on $V^{5+/3+}$ redox couple alone, suggesting that other insertion (*e.g.* conversion) and interface formation processes are likely occurring. Beyond the 5th cycle, Coulombic efficiencies are much improved, and discharge capacity remains relatively stable at around 100 mAh g^{-1}.

In cells with x = 0.5 and 1, results are broadly similar, but with lower initial capacities and more rapid increases in Coulombic efficiency, with $Li_3CrV_2O_8$ still delivering *ca.* 110 mAh g^{-1} at an average working potential of 0.6 V after 50 cycles. Work is continuing to understand the precise nature of the Li insertion mechanism and to optimise performance. The replacement of Ni with Li, Cr appears to improve electrochemical performance with capacities close to that of $Li_4Ti_5O_{12}$ and at significantly lower operating voltages, a potentially significant advantage for negative electrode applications if further performance improvements can be secured.

3.5.3. Reaction mechanisms. The electrochemical behaviour of $Li_{2+x}Ni_{2-2x}Cr_xV_2O_8$ can be understood through two distinct reaction mechanisms depending on the operating voltage range.

Above 3.0 V *vs.* Li^+/Li (positive electrode operation):

The reaction proceeds *via* a topotactic mechanism involving reversible Li^+ extraction/insertion with minimal structural rearrangement:

$$Li_{2+x}Ni_{2-2x}Cr_xV_2O_8 \rightleftharpoons Li_{2+x-y}Ni_{2-2x}Cr_xV_2O_8 + yLi^+ + ye^- \quad (1)$$

This process primarily involves oxidation of Cr^{3+} to Cr^{6+} and Ni^{2+} to Ni^{3+}, as confirmed by our XANES analysis (Fig. 15), though Ni appears to be electrochemically inactive in Cr-rich specimens. However, the migration of Cr^{6+} ions from octahedral 16c to tetrahedral 8a sites during charging blocks the Li^+ conduction pathway, resulting in poor reversibility.

Below 3.0 V *vs.* Li^+/Li (negative electrode operation):

At lower voltages, the reaction mechanism shifts to a conversion-type process involving more extensive structural reorganization:

$$Li_{2+x}Ni_{2-2x}Cr_xV_2O_8 + zLi^+ + ze^- \rightarrow Li_xLi_{2+x}Ni_{2-2x}Cr_xV_2O_8 + \text{conversion products} \quad (2)$$

This process likely involves reduction of V^{5+} to V^{3+} and formation of intermediate phases, accounting for the high initial discharge capacities (>800 mAh g^{-1}) that exceed those possible from simple intercalation mechanisms alone. Further work is ongoing to fully elucidate mechanism (2).

4. Conclusions

The inverse spinel series $Li_{2+x}Ni_{2-2x}Cr_xV_2O_8$ ($0 \le x \le 1$) is reported here for the first time, forming a full solid solution from $LiNiVO_4$ to $Li_3CrV_2O_8$. The family of materials show modest lithium-ion conductivity, with impedance spectroscopy measurements showing total conductivities in the region of 10^{-8} S cm^{-1} at temperatures close to ambient. From neutron diffraction experiments we were able to determine occupancy of a new tetrahedrally-coordinated interstitial 8a site that shares faces with four neighbouring 16c sites, resulting in a three-dimensional 16c–8a–16c Li^+-ion conduction pathway, explaining how modest levels of Li-ion conductivity can be achieved in these inverse spinels even though the 16c site is also partially occupied by Ni and/or Cr. Significant differences in activation energies are observed in results from impedance and muon spectroscopic data, likely due to lithium loss during sintering and the formation of lithium vanadate secondary phases for the bulk pellets used for impedance measurements, where responses were also dominated by grain boundary responses.

Preliminary electrochemical testing and XANES analyses showed reasonable first charge capacities of up to 100 mAh g^{-1} with extremely poor reversibility due to cation mixing of Cr and V over tetrahedral and octahedral sites and the irreversible nature of the $Cr^{3+/6+}$ redox couple. The compositions show more promise as negative electrode materials, with the best performance from the solid solution series observed for $Li_3CrV_2O_8$, delivering discharge capacities of 110 mAh g^{-1} at an average working potential of 0.6 V after 50 cycles. Work is ongoing to further develop this material to improve this discharge capacity and cyclability.

Conflicts of interest

There are no conflicts of interest to declare.

Data availability

All data supporting this publication have been included within the paper, the supplementary information (SI), or are available *via* online repositories at **https://doi.org/10.5286/ISIS.E.RB1920272-1**, **https://doi.org/10.5286/ISIS.E.RB1990195-1** and **https://doi.org/10.5286/ISIS.E.RB2010057-1**. Supplementary information is available. See DOI: **https://doi.org/10.1039/d5cp02385h**.

Acknowledgements

Data collection on the Polaris and Emu instruments at the ISIS Neutron and Muon Source and beamline B18 at the Diamond Light Source were supported by beamtime allocations from the Science and Technology Facilities Council (proposals RB1920272, XB1990195-98, RB2010057 and SP25434). Data files are available from **https://doi.org/10.5286/ISIS.E.RB1920272-1**, **https://doi.org/10.5286/ISIS.E.RB1990195-1** and **https://doi.org/10.5286/ISIS.E.RB2010057-1**. BAA and NRM thank the Lloyds Register Foundation for scholarship funding. We also acknowledge that the PhD work of DZCM and BAA under the supervision of NRM and RB was funded by EPSRC through a Doctoral Training Partnership grant awarded to the University of Sheffield.

References

1 S. G. Booth, A. J. Nedoma, N. N. Anthonisamy, P. J. Baker, R. Boston, H. Bronstein, S. J. Clarke, E. J. Cussen, V. Daramalla, M. De Volder, S. E. Dutton, V. Falkowski, N. A. Fleck, H. S. Geddes, N. Gollapally, A. L. Goodwin, J. M. Griffin, A. R. Haworth, M. A. Hayward, S. Hull, B. J. Inkson, B. J. Johnston, Z. Lu, J. L. MacManus-Driscoll, X. Martínez De Irujo Labalde, I. McClelland, K. McCombie, B. Murdock, D. Nayak, S. Park, G. E. Pérez, C. J. Pickard, L. F. J. Piper, H. Y. Playford, S. Price, D. O. Scanlon, J. C. Stallard, N. Tapia-Ruiz, A. R. West, L. Wheatcroft, M. Wilson, L. Zhang, X. Zhi, B. Zhu and S. A. Cussen, *APL Mater.*, 2021, **9**, 109201.
2 M. Nakayama, R. Jalem and T. Kasuga, *Solid State Ionics*, 2014, **262**, 74–76.
3 T. Ohzuku, A. Ueda and N. Yamamoto, *J. Electrochem. Soc.*, 1995, **142**, 1431.
4 M. Wagemaker, D. R. Simon, E. M. Kelder, J. Schoonman, C. Ringpfeil, U. Haake, D. Lützenkirchen-Hecht, R. Frahm and F. M. Mulder, *Adv. Mater.*, 2006, **18**, 3169–3173.
5 G. T. K. Fey, W. Li and J. R. Dahn, *J. Electrochem. Soc.*, 1994, **141**, 2279.
6 A. K. Padhi, W. B. Archibald, K. S. Nanjundaswamy and J. B. Goodenough, *J. Solid State Chem.*, 1997, **128**, 267–272.
7 G. T. K. Fey and D.-L. Huang, *Electrochim. Acta*, 1999, **45**, 295–314.
8 T. Uyama and K. Mukai, *Mater. Today Energy*, 2019, **14**, 100331.
9 G. Blasse, *J. Inorg. Nucl. Chem.*, 1964, **26**, 1473–1474.
10 J.-C. Joubert and A. Durif-Varambon, *Bull. Mineral.*, 1963, 430.
11 R. I. Smith, S. Hull, M. G. Tucker, H. Y. Playford, D. J. McPhail, S. P. Waller and S. T. Norberg, *Rev. Sci. Instrum.*, 2019, **90**, 115101.
12 O. Arnold, J. C. Bilheux, J. M. Borreguero, A. Buts, S. I. Campbell, L. Chapon, M. Doucet, N. Draper, R. Ferraz Leal, M. A. Gigg, V. E. Lynch, A. Markvardsen, D. J. Mikkelson, R. L. Mikkelson, R. Miller, K. Palmen, P. Parker, G. Passos, T. G. Perring, P. F. Peterson, S. Ren, M. A. Reuter, A. T. Savici, J. W. Taylor, R. J. Taylor, R. Tolchenov, W. Zhou and J. Zikovsky, *Nucl. Instrum. Methods Phys. Res., Sect. A*, 2014, **764**, 156–166.
13 A. C. Larson and R. B. Von Dreele, *Los Alamos National Laboratory Report LAUR*, pp. 86–748, 2000.
14 B. Toby, *J. Appl. Crystallogr.*, 2001, **34**, 210–213.
15 D. Johnson, *Zview for Windows*, Scribner Associates, Inc., Charlesville, Virginia, 2005.
16 B. Ravel and M. Newville, *Phys. Scr.*, 2005, **2005**, 1007.
17 M. Wojdyr, *J. Appl. Crystallogr.*, 2010, **43**, 1126–1128.
18 N. van Landschoot, *Dissertation (TU Delft)*, Universal Press Science Publishers, 2005.
19 A. Kazakopoulos, C. Sarafidis, K. Chrissafis and O. Kalogirou, *Solid State Ionics*, 2008, **179**, 1980–1985.
20 D. Z. C. Martin, A. R. Haworth, W. L. Schmidt, P. J. Baker, R. Boston, K. E. Johnston and N. Reeves-McLaren, *Phys. Chem. Chem. Phys.*, 2019, **21**, 23111–23118.
21 H. Shiiba, M. Nakayama and M. Nogami, *Solid State Ionics*, 2010, **181**, 994–1001.
22 B. Vikram Babu, K. Vijaya Babu, G. Tewodros Aregai, L. Seeta Devi, B. Madhavi Latha, M. Sushma Reddi, K. Samatha and V. Veeraiah, *Results Phys.*, 2018, **9**, 284–289.
23 K. Hoang, *J. Mater. Chem. A*, 2014, **2**, 18271–18280.
24 H. Kawai, M. Tabuchi, M. Nagata, H. Tukamoto and A. R. West, *J. Mater. Chem.*, 1998, **8**, 1273–1280.
25 N. Reeves-Mclaren, R. I. Smith and A. R. West, *Chem. Mater.*, 2011, **23**, 3556–3563.
26 R. S. Liu, Y. C. Cheng, R. Gundakaram and L. Y. Jang, *Mater. Res. Bull.*, 2001, **36**, 1479–1486.

27 N. Ishizawa, D. d Boulay, M. Hayatsu, S. Kuze, Y. Matsushima, H. Ikuta, M. Wakihara, Y. Tabira and J. R. Hester, *J. Solid State Chem.*, 2003, **174**, 167–174.
28 P. J. Baker, I. Franke, F. L. Pratt, T. Lancaster, D. Prabhakaran, W. Hayes and S. J. Blundell, *Phys. Rev. B: Condens. Matter Mater. Phys.*, 2011, **84**, 174403.
29 M. Månsson and J. Sugiyama, *Phys. Scr.*, 2013, **88**, 068509.
30 M. J. Ariza, D. J. Jones, J. Rozière, J. S. Lord and D. Ravot, *J. Phys. Chem. B*, 2003, **107**, 6003–6011.
31 M. Amores, T. E. Ashton, P. J. Baker, E. J. Cussen and S. A. Corr, *J. Mater. Chem. A*, 2016, **4**, 1729–1736.
32 I. McClelland, B. Johnston, P. J. Baker, M. Amores, E. J. Cussen and S. A. Corr, *Annu. Rev. Mater. Res.*, 2020, **50**, 371–393.
33 K. Mukai, J. Sugiyama, Y. Ikedo, H. Nozaki, K. Shimomura, K. Nishiyama, K. Ariyoshi and T. Ohzuku, *J. Power Sources*, 2007, **174**, 711–715.
34 J. Sugiyama, H. Nozaki, I. Umegaki, K. Mukai, K. Miwa, S. Shiraki, T. Hitosugi, A. Suter, T. Prokscha, Z. Salman, J. S. Lord and M. Månsson, *Phys. Rev. B: Condens. Matter Mater. Phys.*, 2015, **92**, 014417.
35 A. Kitajou, J. Yoshida, S. Nakanishi, Y. Matsuda, R. Kanno, T. Okajima and S. Okada, *J. Power Sources*, 2016, **302**, 240–246.
36 F. Farges, *Phys. Chem. Miner.*, 2009, **36**, 463–481.
37 P. Chaurand, J. Rose, V. Briois, M. Salome, O. Proux, V. Nassif, L. Olivi, J. Susini, J.-L. Hazemann and J.-Y. Bottero, *J. Phys. Chem. B*, 2007, **111**, 5101–5110.
38 J. Li, Y. Li, P. K. Routh, E. Makagon, I. Lubomirsky and A. I. Frenkel, *J. Synchrotron Radiat.*, 2021, **28**, 1511–1517.
39 C. Rossignol, G. Ouvrard and E. Baudrin, *J. Electrochem. Soc.*, 2001, **148**, A869.
40 C. Sigala, A. Verbaere, J. L. Mansot, D. Guyomard, Y. Piffard and M. Tournoux, *J. Solid State Chem.*, 1997, **132**, 372–381.
41 R. Kanno, Y. Takeda, M. Hasegawa, Y. Kawamoto and O. Yamamoto, *J. Solid State Chem.*, 1991, **94**, 319–328.

